New synthesis strategies to improve Co-Free $LiNi_{0.5}Mn_{0.5}O_2$ Cathodes: Early transition metal d^0 dopants and Manganese Pyrophosphate Coating

Devendrasinh Darbar, Ethan C. Self, Linze Li, Chongmin Wang, Harry M. Meyer III, Changwook Lee, Jason R. Croy, Mahalingam Balasubramanian, Nitin Muralidharan, Indranil Bhattacharya, Ilias Belharouak, Jagjit Nanda**

D. Darbar, Dr. E.C. Self, Dr. J. Nanda
Chemical Science Divison
Oak Ridge National Laboratory,
Oak Ridge, TN 37831, USA
Corresponding Author Emails: nandaj@ornl.gov (J. Nanda) and selfec@ornl.gov (E. C. Self)

D. Darbar, Dr. I. Bhattacharya
Department of Electrical and Computer Engineering,
Tennessee Technological University,
Cookeville, TN 38505, USA

Dr. J. Nanda, Dr. I. Belharouak
Bredesen Center for Interdisciplinary Research and Graduate Education,
University of Tennessee,
Knoxville, TN 37996, USA

Dr. N. Muralidharan, Dr. I. Belharouak
Energy and Transportation Science Division,
Oak Ridge National Laboratory,
Oak Ridge, TN 37830, USA

Dr. L. Z. Li, Dr. C. M. Wang
Environmental Molecular Sciences Laboratory,
Pacifc Northwest National Laboratory,
Richland, WA 99354, USA

Dr. J. R. Croy.
Chemical Science and Engineering Division,
Argonne National Laboratory,
Argonne, IL,60439, USA

Dr. Changwook Lee, Dr. M. Balasubramanian
X-ray Science Division, Advanced Photon Source,
Argonne National Laboratory,
Argonne, IL,60439, USA

Keywords: Co-free cathodes, d^0 cation, pyrophosphate coating, cation mixing, layered oxide cathodes

Abstract:

In this work, we report solution-based doping and coating strategies to improve the electrochemical performance of the Co-free layered oxide cathode $LiNi_{0.5}Mn_{0.5}O_2$ (NM-50/50). Small amounts of d^0 dopants (e.g., $Mo^{6+}$and Ti^{4+}, 0.5-1 at. %) increase the cathode's specific capacity, cycling stability, and rate capability. For example, a Mo-doped cathode with the nominal composition $LiNi_{0.495}Mn_{0.495}Mo_{0.01}O_2$ exhibits a high reversible capacity of 180 mAh/g at 20 mA/g compared to only 156 mAh/g for undoped NM-50/50. Effects of 1 at.% Mo dopant on the cathode structure have been studied using a suite of characterization tools including X-ray diffraction (XRD), Raman spectroscopy, transmission electron microscopy (TEM), X-ray Photoelectron Spectroscopy (XPS) and X-ray absorption spectroscopy. These measurements demonstrate that Mo^{6+} dopant is enriched near the particle surface and improves the electrochemical performance of $LiNi_{0.5}Mn_{0.5}O_2$ by: (i) reducing Li^+/ Ni^{2+} cation mixing which facilitates Li^+ transport, (ii) mitigating undesirable phase transformations near the cathode surface, and (iii) altering the cathode/electrolyte interfacial chemistry. This work also reports the use of an inorganic $Mn_2P_2O_7$ coating which enhances the cycling stability of Mo-doped NM-50/50, presumably through formation of a stable cathode electrolyte interphase (CEI) layer. Overall, the synthesis approaches reported herein are quite general and can potentially be expanded to other high voltage Li-ion battery cathodes.

1. Introduction

As demand for electric vehicles continues to rise, development of high energy density cobalt free cathodes for Li-ion batteries is critical. $LiNi_{0.5}Mn_{0.5}O_2$ (NM-50/50) has been extensively studied since first reported by Ohzuku and coworkers[1]. A major short coming of such Mn and Ni containing transition metal (TM) layered oxides is related to the high degree of Ni^{2+}/Li^{+} cation mixing. Due to the similar ionic radius of Li^{+} and Ni^{2+}(0.76 and 0.69 Å, respectively), Ni^{2+} typically migrates to 3a sites in the Li layer while Li^{+} migrates to 3b sites in the transition metal (TM) layer[2]. These anti-site defects hinder Li^{+} diffusion throughout the structure which ultimately decreases the cathode's capacity and cycle life. Depending on the synthesis method, pristine NM-50/50 typically has ca. 8-11% anti-site defects[3,4], and the defect concentration increases during electrochemical cycling. One common approach to overcome cation mixing and improve NM-50/50 performance is to substitute Co in the TM layer which facilitates Li^{+} diffusion and increases the active material's electronic conductivity[5].

Breuer et.al. and Susai et.al recently reported[6,7] that substituting a nominal amount (1-3 mol%) of Mo^{6+} in NMC layered cathodes improved the cathode's 1st cycle reversibility, cycle life, and rate performance. DFT calculations showed that Mo^{6+} energetically favors occupying Ni sites. Similarly, our team recently reported on Mo-stabilized NMC cathodes with the general formula $xLi_2MoO_3•(1-x)LiMO_2$ (M = Ni, Mn, Co and $0.10 \leq x \leq 0.15$) in which the Li_2MoO_3 unit improved the material's oxidative stability at high states of charge[8]. In another study, Urban et. al[9] showed that d^0 transition metals (e.g., Ti^{4+}, Mo^{6+}, Zr^{4+} , $V^{5+}$and Nb^{5+}) stabilize cation disordered rock-salt cathodes by allowing Ni^{2+} sites to remain close to their preferred geometry. Atomistic calculations showed that d^0 cations have low energy penalties in the distorted sites which allows other TMs to minimize their distortion.

In this study, we report the effects of two d^0 cations (Ti^{4+} and Mo^{6+}) on the structure and performance of Co-free LMNO cathodes. A primary objective of this work is to determine whether such early TM dopants can reduce Li^{+}/Ni^{2+} cation mixing and thereby improve electrochemical performance. Dopant distribution throughout the particles is also discussed, and we show that enrichment of Mo^{6+} near the particle surface alters the cathode/electrolyte interfacial chemistry. Structural and spectroscopic characterizations of pristine and cycled Mo- and Ti-doped NM-50/50 were performed using a suite of methods including: X-ray diffraction (XRD), Raman spectroscopy, X-ray Photoelectron Spectroscopy (XPS), X-ray absorption spectroscopy (XAS), and high-resolution transmission electron microscopy (HR-TEM). In addition to studying effects of d^0 dopants, an inorganic manganese pyrophosphate ($Mn_2P_2O_7$) coating was applied to Mo-doped NM-50/50 to stabilize the cathode/electrolyte interface at high states of charge. The doping and coating strategies presented here can be applied to a wide range of cathode chemistries to address key issues regarding the bulk structure and cathode/electrolyte interface.

2. Experimental Methods

2.1 Material Synthesis

Cathode Synthesis: For $LiNi_{0.5}Mn_{0.5}O_2$ (NM-50/50)-5g, stoichiometric amounts of $Li(OCOCH_3)_2•2H_2O$ (5 mol% excess), $Ni(OCOCH_3)_2•4H_2O$, $Mn(OCOCH_3)_2•4H_2O$, and citric acid were dissolved in 300 mL deionized water. Detailed quantities of precursors for each cathode are listed in Table S1.The resulting solutions were heated in an oil bath at 60 °C for 35 – 40 hr. while stirring to produce a dry gel. The gel was ground into a fine powder before first phase heating at 400 °C for 4 h in air (5 °C/min ramp rate) followed by second phase heating at 850 °C for 15 h in air (5 °C/min ramp rate). For Mo- and Ti-doped materials, the same procedure was used except for the addition of either $(NH_4)_6Mo_7O_{24}$ (0.5-5 at.% Mo) or TiO_2 (1-5 at.% Ti) to the precursor solution. Nominal stoichiometry of the Mo-doped and Ti-doped NM-50/50 cathodes were $LiNi_{0.5-x/2}Mn_{0.5-x/2}Mo_xO_2$ (x = 0.005 – 0.05) and $LiNi_{0.5-x/2}Mn_{0.5-x/2}Ti_xO_2$ (x = 0.01 – 0.05), respectively.

Manganese Pyrophosphate Coating: Mo-doped NM-50/50 was coated with 2 wt.% $Mn_2P_2O_7$ to stabilize the cathode/electrolyte interface. To prepare the coated cathode, 0.0327 g $Mn(OCOCH_3)_2•4H_2O$ was dissolved in deionized water (10 mL) before adding the as-synthesized 1 at. % Mo-doped NM-50/50 (0.98 g) under continuous stirring (Solution A). Meanwhile, 0.0176 g of $NH_4H_2PO_4$ was dissolved in deionized water (10 mL, Solution B). Solution B was subsequently added dropwise to Solution A within 1 h of continuous stirring. The prepared suspension was dried at 60 °C, and the resulting powder was heated in air at 300 °C for 5 h (2 °C/min ramp rate).

2.2 Material Characterization

X-ray Diffraction (XRD): XRD measurements were conducted on Scintag XDS 2000 powder diffractometer with Cu Kα radiation (λ = 1.5406 Å) in the 2θ range of 10 - 80°. Integrated peak areas were determined using OriginLab software to quantify I(003)/I(104) peak ratios which are related to the degree of cation mixing.

Raman Spectroscopy: Raman spectra were acquired with an Alpha 300 confocal Raman microscope (WITec, GmbH) using a solid-state 532 nm excitation laser, a 20x objective lens, and a grating with 600 grooves per mm. The laser spot size and power were approximately 1 μm^2 and 100 μW, respectively. Raman spectra were analyzed using WITec Project Plus software.

X-ray Photoelectron Spectroscopy (XPS): Samples were placed in a hermetically sealed holder before transferring to the XPS instrument (Thermo Scientific Model K-Alpha XPS) which contained a monochromated, micro-focusing Al K_α X-ray source (1486.6 eV) with a variable X-ray spot size (30 – 400 μm). This work used the 400 μm X-ray spot size to maximize the signal intensity and to obtain an average surface composition over a large area. The instrument used a hemispherical electron energy analyzer equipped with a 128 channel detector system. The base pressure in the analysis chamber was 3×10^{-10} mbar. Wide energy range survey spectra (0 – 1,350 eV) were acquired for qualitative and quantitative analysis using a pass energy setting of 200

eV. To assess the chemical bonding of identified elements, narrow energy range core level spectra were acquired with a pass energy setting of 50 eV. Data were collected and processed using the Thermo Scientific Avantage XPS software package (v 4.61). Spectra were charge corrected using the C 1s core level peak set to 284.8 eV.

X-ray Absorption Spectroscopy (XAS): X-ray absorption fine structure (XAFS) spectroscopy was performed at beamline 20-BM of the Advanced Photon Source. Studies on the Mo dopant were performed in fluorescence mode using a 13-element germanium energy dispersive detector, and the Ni and Mn spectra were obtained using the transmission mode. The X-ray beam was monochromatized using a fixed-exit, double-crystal monochromator. Harmonic rejection was accomplished using a rhodium-coated mirror. Energy calibration was performed using the appropriate metal foil standard. Data reduction and fitting analysis followed standard procedures and was performed using the DEMETER XAFS analysis software[10].

Transmission Electron Microscopy (TEM): Cathode powders were not exposed to any solutions during TEM sample preparation. Post-mortem cathode particles were removed from the current collector and dispensed onto TEM lacey carbon grids inside an Ar-filled glovebox. Scanning transmission electron microscopy (STEM), high-angle annular dark-field (HAADF) imaging, annular bright-field (ABF) imaging, and energy-dispersive X-ray spectroscopy (EDS) mapping were performed on an aberration corrected JEOL JEM-ARM200CF with an operating voltage of 200 kV. The convergence semi-angle was 20.6 mrad, and the signals with semi-angles spanning from 68 – 280 mrad and 8 – 17 mrad were collected for STEM HAADF and STEM ABF imaging, respectively. The EDS data analysis was performed using the software "pathfinder", where the overlapped peaks were deconvolved by using the stored standard reference spectra and employing a multiple, linear least-squares fitting method.

2.3 Electrochemical Measurements

Cathode slurries were prepared by mixing 80 wt.% active material, 10 wt.% Super P carbon black, and 10 wt.% poly (vinylidene fluoride) (PVDF) (80:10:10 by weight) in N-methyl-2-pyrrolidone (NMP). The slurries were cast onto a carbon-coated Al current collector and dried overnight at 80 °C under vacuum. The active material loading in the dried electrodes was ca. 5-6 mg/cm^2. The cathodes electrochemical properties were evaluated in CR2032 half cells containing a Li metal auxiliary/reference electrode. The electrolyte was 1.2M $LiPF_6$ in a mixture of ethylene carbonate (EC) and ethyl methyl carbonate (EMC) (EC:EMC 3:7 by weight). Cells were assembled in an Ar-filled glovebox. Galvanostatic charge/discharge experiments were performed between 2.0-4.5 V at specific currents of 20-200 mA/g using a MACCOR Series 4000 battery tester. Cyclic voltammetry studies were performed between 2.0-4.5 V at scan rates of 0.1 – 1.5 mV/s using a Biologic MPG2 system. For post-mortem analysis, cycled coin cells (terminated in the discharged state, 2.0 V) were dissembled inside an Ar-filled glovebox. The harvested cathodes

were rinsed several times with dimethyl carbonate (DMC) and dried overnight at room temperature under vacuum without air exposure.

3. Results and Discussion

3.1 Electrochemical Properties of d^0-Doped NM-50/50 cathodes

Figure 1 shows the galvanostatic cycling performance of pristine NM-50/50 and NM-50/50 doped with either 1 at.% Mo^{6+} or 1 at.% Ti^{4+}. All cathodes exhibited similar voltage profiles with a sloping plateau ~3.7 - 4.5 V vs. Li/Li^+, indicating charge compensation occurred primarily through the Ni redox center. The initial discharge capacity for Mo-doped NM-50/50 (180 mAh/g) was significantly higher than that of Ti-doped NM-50/50 (155 mAh/g) and undoped NM-50/50 (156 mAh/g). On the other hand, Ti-doped NM-50/50 exhibited superior cycling stability with ~77% capacity retention after 100 cycles compared to 65% and 63% retention for Mo-doped NM-50/50 and undoped NM-50/50, respectively (see Figure 1a). The effect of Mo^{6+} and Ti^{4+} dopant concentration on cycling performance is shown in Figure S1. It is noteworthy that higher Mo dopant levels (3-5 at.%) negatively impacted electrochemical performance due to formation of impurity phases (e.g., Li_2MoO_4 and Mn_2O_3 as shown in Figure S3 and discussed later in the text). While a wide range of cathode compositions can be prepared using the sol-gel processing route reported here, the remainder of this work largely focuses on characterization of NM-50/50 doped with 1 at.% Mo.

The higher capacity of 1 at. % Mo-doped NM-50/50 is partially attributed to faster Li^+ transport through the cathode structure as a result of fewer Li^+/Ni^{2+} anti-site defects (as is shown later via XRD and TEM measurements). To quantify Li^+ transport in NM-50/50 and Mo-doped NM-50/50, apparent Li^+ diffusion coefficients were estimated using cyclic voltammetry and a Randles-Sevcik analysis (see Figure S2). Compared to NM-50/50, Mo-doped NM-50/50 exhibited higher specific currents (normalized by the active material mass) at a given scan rate which is consistent with the higher gravimetric capacities measured during galvanostatic cycling. Figure S2c shows that the anodic peak currents varied linearly with the square root of the scan rate, which is a hallmark of a diffusion-controlled process. Based on this analysis, the Li^+ diffusivity for Mo-doped NM-50/50 was ~3-fold greater than that of undoped NM-50/50 ($6.7x10^{-9}$ and $2.9x10^{-9}$ cm^2/s, respectively, see Table S2). It is important to note that these results should only be used for qualitative comparisons of Li^+ transport in undoped vs. Mo-doped NM-50/50 since the electrochemically active surface area of the porous electrodes is not known. Nonetheless, the results in Figures 1, S1, and S2 clearly demonstrate that small amounts of d^0 dopants have a positive impact on the electrochemical performance of NM-50/50 cathodes. To better understand these effects, a primary focus of this study is to evaluate how 1 at.% Mo dopant affects the cathode's structure before and after cycling.

3.2 Structural Characterization of Pristine and Mo-Doped NM-50/50

XRD patterns of NM-50/50 and 1 at. % Mo-doped NM-50/50 are given in Figure 2a. The cathodes had the expected hexagonal layered structure with trigonal symmetry (space group $R\bar{3}m$, see Figure 2b), and the broad peak near 2θ = ~22° corresponds to a monoclinic Li_2MnO_3 structure. 1 at.% Mo-doped NM-50/50 showed no impurities within the diffractometer's sensitivity limits, but higher Mo dopant levels (3 and 5 at.%) resulted in Li_2MoO_4 and Mn_3O_4 impurities (see Figure S3) which may be the reason for the lower capacity of these materials (Figure S1). The relative intensity of the (003) and (104) peaks provides a qualitative assessment of Li^+/Ni^{2+} cation mixing where a higher I(003)/I(104) ratio is indicative of fewer anti-site defects[11]. Doping NM-50/50 with 1 at% Mo increased the I(003)/I(104) ratio from 0.53 to 0.56 which suggests that Mo doping slightly decreased the extent of cation mixing. This finding is consistent with our previous report on Mo-doped NM-50/50 studied using STEM.[12]

Figure S4 shows the Raman spectra of NM-50/50 and 1 at.% Mo-doped NM-50/50 electrode. $LiMO_2$ layered oxide cathodes typically contain two Raman active vibrational modes between 400-700 cm^{-1}, A_{1g} and E_g which correspond to M-O symmetrical stretching and O-M-O bending, respectively[6,13]. These features are consistent with the Raman analysis of $LiNi_{0.5}Mn_{0.5}O_2$ cathodes reported previously[14,15]. D and G bands of the conductive carbon additive were detected at ~1350 and ~1600 cm^{-1}, respectively[16]. No additional Raman-active vibrational modes were detected for Mo-doped NM-50/50 which confirms that the material contained no/few phase impurities. Similarly, the lack of distinct Mo-O bands is attributed to instrument sensitivitiy limits and the low dopant content.

X-ray photoelectron spectroscopy (XPS) and X-ray absorption edge energy spectroscopy (XAS) experiments were performed to determine the transition metal oxidation states near the cathode surface and in the bulk, respectively. Figure 3a shows the XPS survey scans for NM-50/50 and Mo-doped NM-50/50 with all the expected core level signals including Li 1s, Ni 2p, Mn 2p, O 1s, and Mo 3d. Figure 3b shows the Mo 3d core level spectra for Mo-doped NM-50/50 with $3d_{5/2}$ and $3d_{3/2}$ peaks at binding energies of 232.7 and 235.6 eV, respectively. These features are similar to that of MoO_3 which indicates Mo is primarily in the +6 oxidation state.[17–19]. The 2p core level spectra for Mn and Ni (Figure 3c, 3d) exhibited the usual spin-orbit doublets corresponding to $2p_{1/2}$ and $2p_{3/2}$. For Mn 2p, there was no binding energy shift between NM-50/50 and Mo-doped NM-50/50, and Mn $2p_{1/2}$ and Mn $2p_{3/2}$ peaks were at 653.8eV and 642.4 eV, respectively. These features are similar to that of MnO_2,[20–25] indicating Mn has an average oxidation state of +4 in both cathodes. Similarly, the Ni $2p_{3/2}$ peak in NM-50/50 and Mo-doped NM-50/50 had a binding energy of 855 eV with a satellite peak at 861 eV which is consistent with the presence of Ni^{+2} [26]. Interestingly, as shown in Table S3, the Mo dopant content near the surface was ~18× higher than expected based on the nominal bulk stoichiometry. This discrepancy is attributed to the surface sensitivity of XPS which only probes depths of approximately 50-70Å [27].This finding suggests that, in addition to decreases in Li^+/Ni^{2+} cation mixing, the improved performance of the Mo-doped NM-50/50 is partially due to changes in the cathode/electrolyte interfacial chemistry.

The oxidation state and electronic structure of transition metals in Mo-doped NM-50/50 were also evaluated using X-ray absorption spectroscopy. Figures 4a and 4b show Mo K-edge X-ray absorption near edge structure (XANES) and extended X-ray absorption fine structure (EXAFS) data (presented as a k^3-weighted Fourier transform) for Mo-doped NM-50/50 compared with that of Li_2MoO_3 and Li_2MoO_4 standards containing Mo^{4+} and Mo^{6+}, respectively. The pre-edge and absorption edge position of Mo-doped NM-50/50 are similar to that of Li_2MoO_4 which confirms the cathode contains Mo^{6+} [28]. The high intensity of the pre-edge peak strongly suggests that the Mo dopant is present predominantly as a tetrahedrally coordinated $(MoO_4)^{2-}$ entity, similar to the nature of Mo in the standard Li_2MoO_4. EXAFS analysis shows that there are ~ 3.2 (3) oxygen neighbors at a distance ~1.762 (8) Å in the first coordination shell. No evidence for higher shell scattering is present in the data. The slight reduction from the expected coordination number for a tetrahedrally-coordinated moiety (3.2 vs. 4) may be due to some under coordination at the oxide surface or the presence of a distorted local environment that lowers the apparent coordination number. These findings indicate that the Mo dopant exists either: (i) as a surface species which is tetrahedrally coordinated with oxygen and/or (ii) in tetrahedral interstitial sites in the bulk $R\bar{3}m$ structure.

Figure S5 shows XANES data at the Ni K-edge and the Mn K-edge for NM-50/50 and Mo-doped NM-50/50. Notably, the Mo dopant did not induce any significant energy shifts at either the Ni or Mn K-edges which indicates that introducing Mo^{6+} did not substantially impact the average Mn and Ni oxidation states[29–31]. Given the small amount of Mo doping (1 at.%), this is not an unexpected result. It is plausible that introducing a high valence dopant (e.g., Mo^{6+}) may locally reduce Ni and/or Mn cations, but such an investigation is outside the scope of this study. Any potential changes in Ni/Mn oxidation states are small and beyond the sensitivity of the bulk averaged XANES data.

3.3 Post-Mortem Analysis of Mo-Doped NM-50/50

Capacity and voltage fade of layered oxide cathodes during cycling has been correlated with irreversible phase transformations near the surface and/or throughout the bulk[32,33]. Figures 5a and 5b show HAADF STEM images of near surface regions for NM-50/50 and Mo-doped NM-50/50 after 100 charge/discharge cycles. In NM-50/50, structural rearrangements after cycling include: (i) formation of spinel and rocksalt phases near the particle surface and (ii) higher Li^+/Ni^{2+} cation mixing within the layered structures as evidenced by the enhanced image intensity in the Li layers. On the other hand, Mo doping mitigated cycling-induced cation mixing and layered-to-spinel/rocksalt structural transformations which improved the cathode's electrochemical performance compared to NM-50/50 (Figure 1).

Ex-situ XPS measurements provide additional insights on how the surface chemistry of Mo-doped NM-50/50 changed after cycling. Figure 5c shows that the cycled electrode exhibited broader Mo 3d features compared to the pristine cathode. This broadening is attributed to the presence of more diverse local bonding environments, possibly due to the layered-to-spinel phase

transformation shown in Figure 5b. Furthermore, increased intensity of the Mo $3d_{5/2}$ peak near 234 eV suggests the presence of F-Mo-F species (e.g., from decomposition of $LiPF_6$ and/or PVDF) in the cathode electrolyte interphase (CEI) layer[6]. The CEI layer's composition was further evaluated from the O1s, C1s, and F1s core level spectra shown in Figure 6. The peaks near 287-288 eV in the C1s spectrum (Figure 6a) and 533-534 eV in the O 1s spectrum (Figure 6b) are attributed to species containing O=C-O and C=O functionalities due to electrolyte oxidation at high states of charge[34–36]. Similarly, LiF from $LiPF_6$ decomposition was detected on the cycled electrode's surface as shown in the F 1s spectrum (Figure 6c)[37,38]. Overall, these findings indicate the CEI layer on Mo-doped NM-50/50 is a complex passive film consisting of organic and inorganic species which is similar to that reported for conventional metal oxide cathodes[39,40].

3.4 Manganese Pyrophosphate ($Mn_2P_2O_7$) Coating on Mo-Doped LMNO

The capacity fade for Mo-doped NM-50/50 during cycling (Figure 1) is attributed to changes in the bulk structure (e.g., layered-to-spinel phase transformation) and instabilities at the cathode/electrolyte interface. To encourage formation of a more stable CEI layer, we developed a solution-based processing route to coat $Mn_2P_2O_7$ on Mo-doped NM-50/50. Figure 7a shows an XRD pattern of Mo-doped NM-50/50 powder coated with 2 wt.% $Mn_2P_2O_7$. These results demonstrate that the coating process did not have a major impact on the cathode's bulk structure. No Bragg reflections assigned to $Mn_2P_2O_7$ were detected which is due to: (i) the low loading of the $Mn_2P_2O_7$ coating (~1.5 nm thick) and (ii) the coating's largely amorphous structure as shown by the STEM ABF image in Figure 7b. STEM-EDS elemental maps of the coated cathode (Figure 7c) indicate that phosphorus (and therefore the $Mn_2P_2O_7$ coating) was uniformly distributed on the particle's surface.

Galvanostatic cycling data for Mo-doped NM-50/50 with and without the $Mn_2P_2O_7$ coating is shown in Figure 7d. The coating had negligible impact on the initial reversible capacity (~180 mAh/g at 20 mA/g) but substantially increased the initial coulombic efficiency (~95 and ~91% for coated and uncoated Mo-doped NM-50/50, respectively). While most of the capacity for the coated Mo-doped NM-50/50 was due to the Ni redox center, the $Mn_2P_2O_7$ coating showed some electrochemical activity and contributed ~10mAh/g near 3.0 V vs. Li/Li^+ (see Figure S6a). This feature is attributed to $Mn^{3+/4+}$ redox as was recently reported for NMC442 coated with $MnPO_4$[41]. Importantly, the coated cathode exhibited significantly better cycling stability with 78% capacity retention after 100 cycles compared to 65% for Mo-doped NM-50/50 and 63% for undoped NM-50/50. The coated cathode also showed superior rate capabilities with ~35% higher capacity than uncoated Mo-doped NM-50/50 at 200 mA/g (see Figure S6b). We postulate that the $Mn_2P_2O_7$ coating promoted better electrochemical performance by: (i) mitigating detrimental side reactions at cathode/electrolyte interface, (ii) forming a more ionically conductive CEI film, and/or (iii) preventing the dissolution of the transition metal cations into the electrolyte. Detailed studies related to the coating's role on electrochemical performance are under investigation.

4. Conclusion

Development of high energy density Co-free cathodes is critical to meet ever-growing demands for Li-ion batteries. This work demonstrates that the electrochemical performance of Co-free $LiNi_{0.5}Mn_{0.5}O_2$ (NM-50/50) layered oxide cathodes is significantly improved by incorporating d^0 transition metal dopants (i.e., Mo^{6+} and Ti^{4+}) and applying inorganic coatings (i.e., $Mn_2P_2O_7$) using scalable solution-based processing routes. Doping NM-50/50 with 1 at.% Mo ($LiNi_{0.495}Mn_{0.495}Mo_{0.01}O_2$) decreased the amount of Li^+/Ni^{2+} anti-site defects which promoted higher Li^+ diffusivity and reversible capacity (e.g., 180 mAh/g for Mo-doped NM-50/50 compared to 156 mAh/g for undoped NM-50/50). The improved electrochemical performance of the Mo-doped NM-50/50 is also attributed to changes in the cathode/electrolyte interfacial chemistry due to enrichment of Mo near the particle surface. In addition to studying the effects of d^0 dopants on NM-50/50, we demonstrate that the cathode/electrolyte interface can be stabilized by applying a thin $Mn_2P_2O_7$ coating (~1.5 nm thick) which improved cycling stability considerably (e.g., 78 vs. 65% capacity retention after 100 cycles for coated and uncoated Mo-doped NM-50/50, respectively). Overall, the doping and coating strategies presented here are quite general and can be applied to a wide range of cathode chemistries to address key issues which limit energy density and cycle life.

ASSOCIATED CONTENT

Supporting Information. Supporting information contains additional results including XRD, XPS, XAS, electrochemical testing, and calculation of apparent Li^+ diffusivity. This material is available free of charge.

AUTHOR INFORMATION

Corresponding authors

*Email: nandaj@ornl.gov (J. Nanda)

selfec@ornl.gov (E. C. Self)

ACKNOWLEDGMENT

This research at Oak Ridge National Laboratory, managed by UT-Battelle, LLC and was sponsored by the Energy Efficiency and Renewable Energy (EERE), Vehicle Technologies Office (VTO). This research used resources of the Advanced Photon Source, a U.S. Department of Energy (DOE) Office of Science User Facility operated for the DOE Office of Science by Argonne National Laboratory under Contract No. DE-AC02-06CH11357. Electron Microscopy work was supported by Energy Efficiency and Renewable Energy (EERE), Vehicle Technologies Office

(VTO) and was conducted in the William R. Wiley Environmental Molecular Sciences Laboratory (EMSL), a national scientific user facility sponsored by DOE's Office of Biological and Environmental Research and located at PNNL.

5. References

(1) Ohzuku, T.; Makimura, Y. Layered Lithium Insertion Material of $LiNi_{1/2}Mn_{1/2}O_2$: A Possible Alternative to $LiCoO_2$ for Advanced Lithium-Ion Batteries. *Chem. Lett.* **2001**, *30* (8), 744–745. https://doi.org/10.1246/cl.2001.744.

(2) Zheng, J.; Ye, Y.; Liu, T.; Xiao, Y.; Wang, C.; Wang, F.; Pan, F. Ni/Li Disordering in Layered Transition Metal Oxide: Electrochemical Impact, Origin, and Control. *Acc. Chem. Res.* **2019**, *52* (8), 2201–2209. https://doi.org/10.1021/acs.accounts.9b00033.

(3) Venkatraman, S.; Manthiram, A. Structural and Chemical Characterization of Layered Li1-XNi 1-YMnyO2-δ (y = 0.25 and 0.5, and $0 \leq (1 - x) \leq 1$) Oxides. *Chem. Mater.* **2003**, *15* (26), 5003–5009. https://doi.org/10.1021/cm034757b.

(4) Arachi, Y.; Kobayashi, H.; Emura, S.; Nakata, Y.; Tanaka, M.; Asai, T. Structural Change of $Li_{1-x}Ni_{0.5}Mn_{0.5}O_2$ Cathode Materials for Lithium-Ion Batteries by Synchrotron Radiation. *Chem. Lett.* **2003**, *32* (1), 60–61. https://doi.org/10.1246/cl.2003.60.

(5) Ohzuku, T.; Makimura, Y. Layered Lithium Insertion Material of LiCo1/3Ni1/3Mn1/3O2 for Lithium-Ion Batteries. *Chem. Lett.* **2001**, No. 7, 642–643. https://doi.org/10.1246/cl.2001.642.

(6) Breuer, O.; Chakraborty, A.; Liu, J.; Kravchuk, T.; Burstein, L.; Grinblat, J.; Kauffman, Y.; Gladkih, A.; Nayak, P.; Tsubery, M.; et al. Understanding the Role of Minor Molybdenum Doping in LiNi0.5Co0.2Mn0.3O2 Electrodes: From Structural and Surface Analyses and Theoretical Modeling to Practical Electrochemical Cells. *ACS Appl. Mater. Interfaces* **2018**, *10* (35), 29608–29621. https://doi.org/10.1021/acsami.8b09795.

(7) Susai, F. A.; Kovacheva, D.; Chakraborty, A.; Kravchuk, T.; Ravikumar, R.; Talianker, M.; Grinblat, J.; Burstein, L.; Kauffmann, Y.; Major, D. T.; et al. Improving Performance of LiNi0.8Co0.1Mn0.1O2 Cathode Materials for Lithium-Ion Batteries by Doping with Molybdenum-Ions: Theoretical and Experimental Studies. *ACS Appl. Energy Mater.* **2019**, *2* (6), 4521–4534. https://doi.org/10.1021/acsaem.9b00767.

(8) Self, E. C.; Zou, L.; Zhang, M. J.; Opfer, R.; Ruther, R. E.; Veith, G. M.; Song, B.; Wang, C.; Wang, F.; Huq, A.; et al. Synthesis and Electrochemical and Structural Investigations

of Oxidatively Stable Li2MoO3 and XLi2MoO3·(1 - X)LiMO2 Composite Cathodes. *Chem. Mater.* **2018**, *30* (15), 5061–5068. https://doi.org/10.1021/acs.chemmater.8b01408.

(9) Urban, A.; Abdellahi, A.; Dacek, S.; Artrith, N.; Ceder, G. Electronic-Structure Origin of Cation Disorder in Transition-Metal Oxides. *Phys. Rev. Lett.* **2017**, *119* (17). https://doi.org/10.1103/PhysRevLett.119.176402.

(10) Ravel, B.; Newville, M. ATHENA, ARTEMIS, HEPHAESTUS: Data Analysis for X-Ray Absorption Spectroscopy Using IFEFFIT. In *Journal of Synchrotron Radiation*; International Union of Crystallography, 2005; Vol. 12, pp 537–541. https://doi.org/10.1107/S0909049505012719.

(11) Ohzuku, T.; Ueda, A.; Nagayama, M.; Iwakoshi, Y.; Komori, H. Comparative Study of LiCoO2, LiNi1 2Co1 2O2 and LiNiO2 for 4 Volt Secondary Lithium Cells. *Electrochim. Acta* **1993**, *38* (9), 1159–1167. https://doi.org/10.1016/0013-4686(93)80046-3.

(12) Li, L.; Yu, J.; Darbar, D.; Self, E. C.; Wang, D.; Nanda, J.; Bhattacharya, I.; Wang, C. Atomic-Scale Mechanisms of Enhanced Electrochemical Properties of Mo-Doped Co-Free Layered Oxide Cathodes for Lithium-Ion Batteries. *ACS Energy Lett.* **2019**, *4* (10), 2540–2546. https://doi.org/10.1021/acsenergylett.9b01830.

(13) Zhang, X.; Mauger, A.; Lu, Q.; Groult, H.; Perrigaud, L.; Gendron, F.; Julien, C. M. Synthesis and Characterization of LiNi1/3Mn1/3Co 1/3O2 by Wet-Chemical Method. *Electrochim. Acta* **2010**, *55* (22), 6440–6449. https://doi.org/10.1016/j.electacta.2010.06.040.

(14) Julien, C. Local Cationic Environment in Lithium Nickel–Cobalt Oxides Used as Cathode Materials for Lithium Batteries. *Solid State Ionics* **2000**, *136–137*, 887–896. https://doi.org/10.1016/S0167-2738(00)00503-8.

(15) Xia, H.; Meng, Y. S.; Lai, M. O.; Lu, L. Structural and Electrochemical Properties of LiNi[Sub 0.5]Mn[Sub 0.5]O[Sub 2] Thin-Film Electrodes Prepared by Pulsed Laser Deposition. *J. Electrochem. Soc.* **2010**, *157* (3), A348. https://doi.org/10.1149/1.3294719.

(16) Knight, D. S.; White, W. B. Characterization of Diamond Films by Raman Spectroscopy. *J. Mater. Res.* **1989**, *4* (2), 385–393. https://doi.org/10.1557/JMR.1989.0385.

(17) Shimoda, M.; Hirata, T.; Yagisawa, K.; Okochi, M.; Yoshikawa, A. Deconvolution of Mo 3d X-Ray Photoemission Spectraγ-Mo4O11: Agreement with Prediction from Bond Length-Bond Strength Relationships. *J. Mater. Sci. Lett.* **1989**, *8* (9), 1089–1091. https://doi.org/10.1007/BF01730497.

(18) Kim, K. S.; Baitinger, W. E.; Amy, J. W.; Winograd, N. ESCA Studies of Metal-Oxygen Surfaces Using Argon and Oxygen Ion-Bombardment. *J. Electron Spectros. Relat. Phenomena* **1974**, *5* (1), 351–367. https://doi.org/10.1016/0368-2048(74)85023-1.

(19) Swartz, W.; Hercules, D. M. X-Ray Photoelectron Spectroscopy of Molybdenum Compounds. Use of Electron Spectroscopy for Chemical Analysis (ESCA) in Quantitative Analysis. *Anal. Chem.* **1971**, *43* (13), 1774–1779. https://doi.org/10.1021/ac60307a020.

(20) Carver, J. C.; Schweitzer, G. K.; Carlson, T. A. Use of X-Ray Photoelectron Spectroscopy to Study Bonding in Cr, Mn, Fe, and Co Compounds. *J. Chem. Phys.* **1972**, *57* (2), 973–982. https://doi.org/10.1063/1.1678348.

(21) Di Castro, V.; Polzonetti, G. XPS Study of MnO Oxidation. *J. Electron Spectros. Relat. Phenomena* **1989**, *48* (1), 117–123. https://doi.org/10.1016/0368-2048(89)80009-X.

(22) Oku, M.; Hirokawa, K.; Ikeda, S. X-Ray Photoelectron Spectroscopy of Manganese—Oxygen Systems. *J. Electron Spectros. Relat. Phenomena* **1975**, *7* (5), 465–473. https://doi.org/10.1016/0368-2048(75)85010-9.

(23) Hsin-Kuei, H.; Rabalais, J. W. Chemisorption and the Initial Stage of Oxidation on Mn. *Surf. Sci.* **1981**, *107* (2–3), 376–390. https://doi.org/10.1016/0039-6028(81)90533-1.

(24) Foord, J. S.; Jackman, R. B.; Allen, G. C. An X-Ray Photoelectron Spectroscopic Investigation of the Oxidation of Manganese. *Philos. Mag. A* **1984**, *49* (5), 657–663. https://doi.org/10.1080/01418618408233293.

(25) Moses Ezhil Raj, A.; Victoria, S. G.; Jothy, V. B.; Ravidhas, C.; Wollschläger, J.; Suendorf, M.; Neumann, M.; Jayachandran, M.; Sanjeeviraja, C. XRD and XPS Characterization of Mixed Valence Mn3O4 Hausmannite Thin Films Prepared by Chemical Spray Pyrolysis Technique. *Appl. Surf. Sci.* **2010**, *256* (9), 2920–2926. https://doi.org/10.1016/J.APSUSC.2009.11.051.

(26) Gopukumar, S.; Yoon Chung, K.; Kim, K. B. Novel Synthesis of Layered LiNi 1/2 Mn 1/2 O 2 as Cathode Material for Lithium Rechargeable Cells. *Electrochim. Acta* **2004**, *49*, 803–810. https://doi.org/10.1016/j.electacta.2003.09.034.

(27) Welker, R. W. Size Analysis and Identification of Particles. In *Developments in Surface Contamination and Cleaning: Detection, Characterization, and Analysis of Contaminants*; Elsevier Inc., 2012; pp 179–213. https://doi.org/10.1016/B978-1-4377-7883-0.00004-3.

(28) Farges, F.; Siewert, R.; Brown, G. E.; Guesdon, A.; Morin, G. Structural Environments around Molybdenum in Silicate Glasses and Melts. I. Influence of Composition and Oxygen Fugacity on the Local Structure of Molybdenum. *Can. Mineral.* **2006**, *44* (3), 731–753. https://doi.org/10.2113/gscanmin.44.3.731.

(29) Croy, J. R.; Kang, S. H.; Balasubramanian, M.; Thackeray, M. M. Li2MnO3-Based Composite Cathodes for Lithium Batteries: A Novel Synthesis Approach and New Structures. *Electrochem. commun.* **2011**, *13* (10), 1063–1066. https://doi.org/10.1016/j.elecom.2011.06.037.

(30) Karan, N. K.; Abraham, D. P.; Balasubramanian, M.; Furczon, M. M.; Thomas, R.; Katiyar, R. S. Morphology, Structure, and Electrochemistry of Solution-Derived LiMn 0.5−x Cr 2x Ni 0.5−x O 2 for Lithium-Ion Cells. *J. Electrochem. Soc.* **2009**, *156*, 553–562. https://doi.org/10.1149/1.3125702.

(31) Croy, J. R.; Gallagher, K. G.; Balasubramanian, M.; Long, B. R.; Thackeray, M. M. Quantifying Hysteresis and Voltage Fade in XLi 2 MnO 3 • (1-x)LiMn 0.5 Ni 0.5 O 2 Electrodes as a Function of Li 2 MnO 3 Content. *J. Electrochem. Soc.* **2014**, *161* (3), 318–

325. https://doi.org/10.1149/2.049403jes.

(32) Gu, M.; Belharouak, I.; Zheng, J.; Wu, H.; Xiao, J.; Genc, A.; Amine, K.; Thevuthasan, S.; Baer, D. R.; Zhang, J.-G.; et al. Formation of the Spinel Phase in the Layered Composite Cathode Used in Li-Ion Batteries. *ACS Nano* **2013**, *7* (1), 760–767. https://doi.org/10.1021/nn305065u.

(33) Lin, F.; Markus, I. M.; Nordlund, D.; Weng, T. C.; Asta, M. D.; Xin, H. L.; Doeff, M. M. Surface Reconstruction and Chemical Evolution of Stoichiometric Layered Cathode Materials for Lithium-Ion Batteries. *Nat. Commun.* **2014**, *5*, 3529. https://doi.org/10.1038/ncomms4529.

(34) Yang, L.; Ravdel, B.; Lucht, B. L. Electrolyte Reactions with the Surface of High Voltage LiNi 0.5Mn1.5O4 Cathodes for Lithium-Ion Batteries. *Electrochem. Solid-State Lett.* **2010**, *13* (8), A95. https://doi.org/10.1149/1.3428515.

(35) Lindgren, F.; Xu, C.; Niedzicki, L.; Marcinek, M.; Gustafsson, T.; Björefors, F.; Edström, K.; Younesi, R. SEI Formation and Interfacial Stability of a Si Electrode in a LiTDI-Salt Based Electrolyte with FEC and VC Additives for Li-Ion Batteries. *ACS Appl. Mater. Interfaces* **2016**, *8* (24), 15758–15766. https://doi.org/10.1021/acsami.6b02650.

(36) Björklund, E.; Brandell, D.; Hahlin, M.; Edström, K.; Younesi, R. How the Negative Electrode Influences Interfacial and Electrochemical Properties of LiNi 1/3 Co 1/3 Mn 1/3 O 2 Cathodes in Li-Ion Batteries . *J. Electrochem. Soc.* **2017**, *164* (13), A3054–A3059. https://doi.org/10.1149/2.0711713jes.

(37) Im, J.; Lee, J.; Ryou, M.-H.; Lee, Y. M.; Cho, K. Y. Fluorinated Carbonate-Based Electrolyte for High-Voltage Li(Ni 0.5 Mn 0.3 Co 0.2)O 2 /Graphite Lithium-Ion Battery . *J. Electrochem. Soc.* **2017**, *164* (1), A6381–A6385. https://doi.org/10.1149/2.0591701jes.

(38) Eriksson, T.; Andersson, A. M.; Gejke, C.; Gustafsson, T.; Thomas, J. O. Influence of Temperature on the Interface Chemistry of LixMn2O4 Electrodes. *Langmuir* **2002**, *18* (9), 3609–3619. https://doi.org/10.1021/la011354m.

(39) XPS Identification of the Organic and Inorganic Components of the Electrode/Electrolyte Interface Formed on a Metallic Cathode. **2005**. https://doi.org/10.1149/1.1861994.

(40) Edström, K.; Gustafsson, T.; Thomas, J. O. The Cathode-Electrolyte Interface in the Li-Ion Battery. In *Electrochimica Acta*; Pergamon, 2004; Vol. 50, pp 397–403. https://doi.org/10.1016/j.electacta.2004.03.049.

(41) Chen, Z.; Kim, G. T.; Bresser, D.; Diemant, T.; Asenbauer, J.; Jeong, S.; Copley, M.; Behm, R. J.; Lin, J.; Shen, Z.; et al. MnPO4-Coated Li(Ni0.4Co0.2Mn0.4)O2 for Lithium(-Ion) Batteries with Outstanding Cycling Stability and Enhanced Lithiation Kinetics. *Adv. Energy Mater.* **2018**, *8* (27). https://doi.org/10.1002/aenm.201801573.

Graphical Abstract

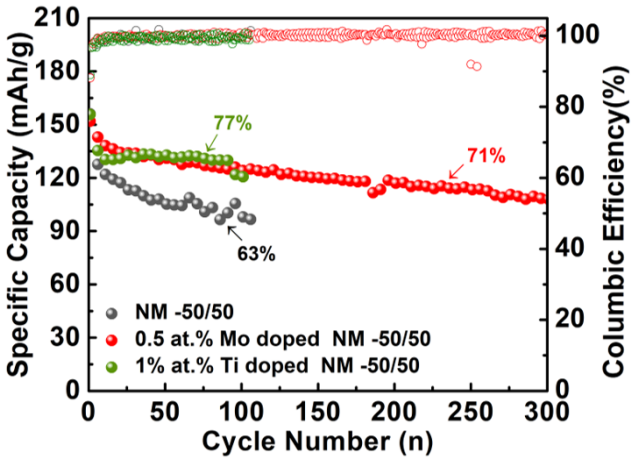

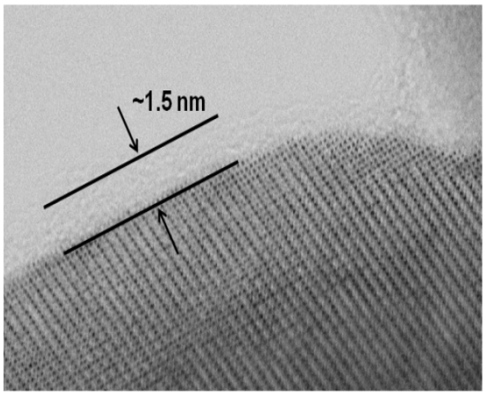

- **Electrochemical performances for d^0 cation doped NM-50/50.**
- **Amorphous pyrophosphate ($Mn_2P_2O_7$) coating on d^0 cation doped NM-50/50 to prevent the instability of cathode electrolyte interface.**

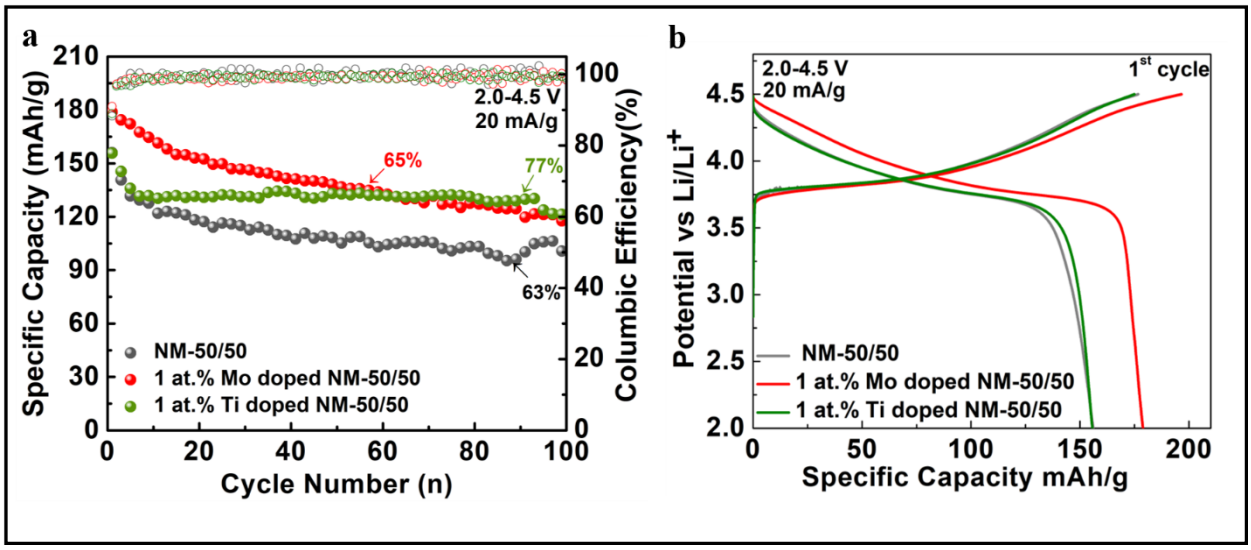

Figure 1. Electrochemical performance of NM-50/50, 1 at.% Mo-doped NM-50/50, and 1 at.% Ti-doped NM-50/50 cathodes. (a) Specific capacity vs. cycle number for cathodes cycled between 2.0 – 4.5 V vs. Li/Li^+ at a specific current of 20 mA/g. (b) Charge/discharge curves collected during the 1st cycle for undoped and doped cathodes. Low levels of d^0 cation dopants significantly improved the capacity and/or cycle life of NM-50/50.

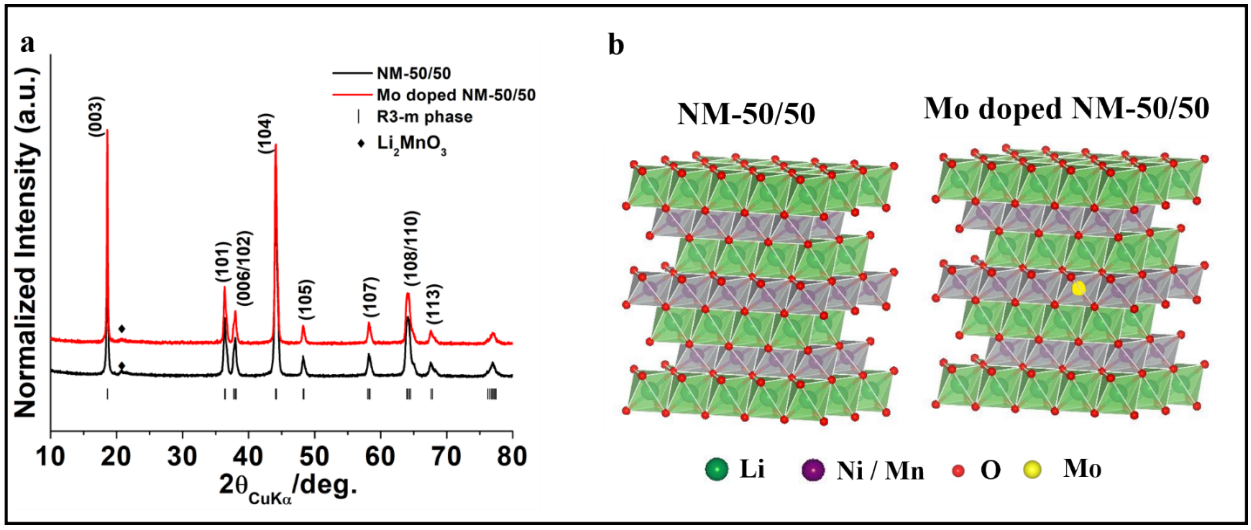

Figure 2. Structural analysis of NM-50/50 and Mo-doped NM-50/50 showing (a) X-ray diffraction (XRD) patterns, (b) crystallographic structure of the cathodes.

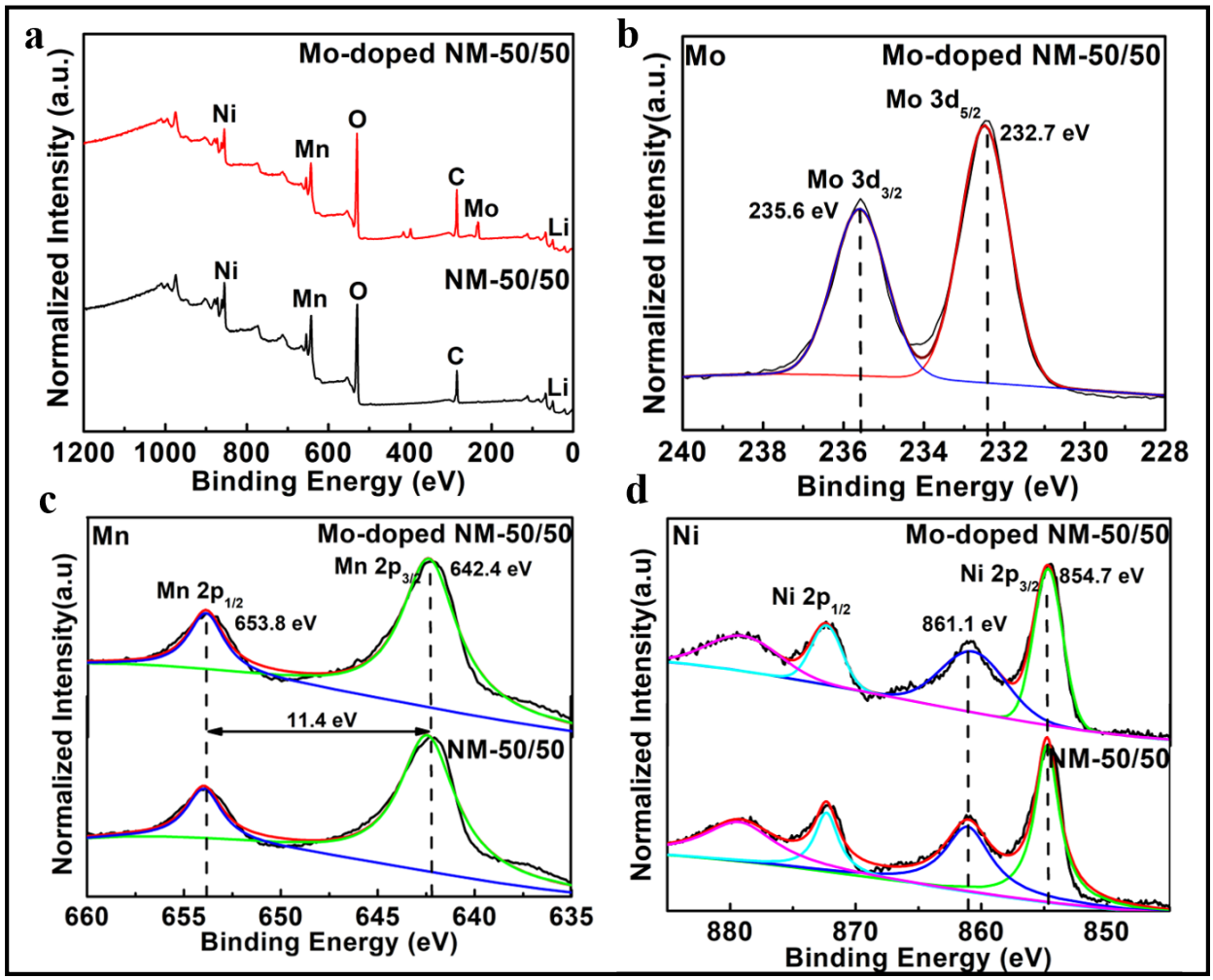

Figure 3. X-ray photoelectron spectroscopy (XPS) analysis of NM-50/50 and Mo-doped NM-50/50 powders before cycling. (a) Survey spectra and (b-d) core-level spectra showing (b) Mo 3d, (c) Mn 2p, and (d) Ni 2p.

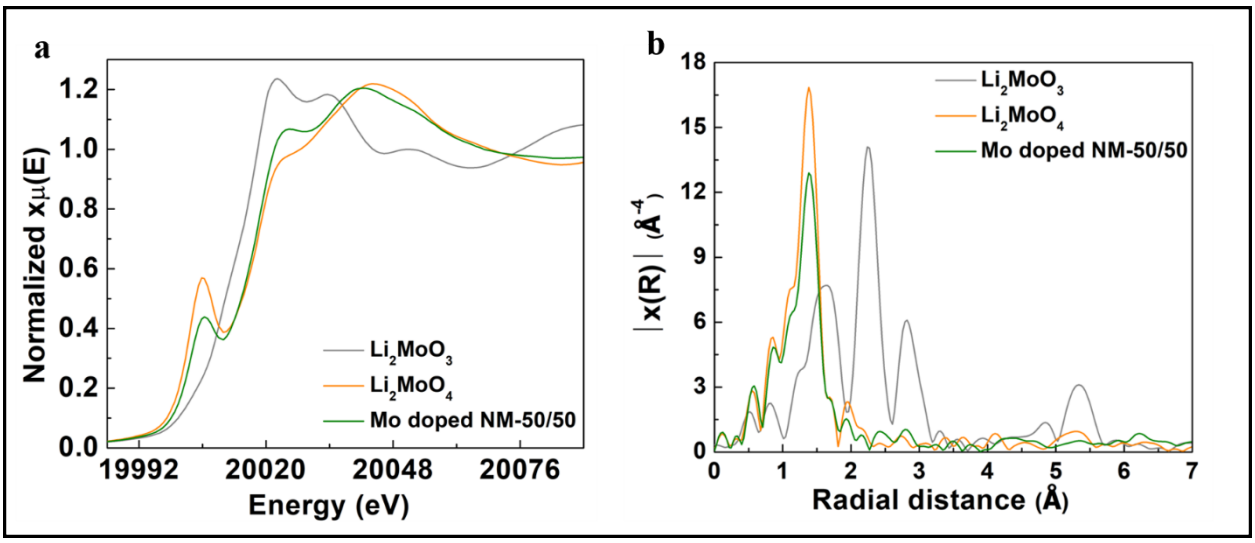

Figure 4. X-ray absorption spectroscopy (XAS) data for NM-50/50 and Mo-doped NM-50/50. (a) Mo K-edge X-ray Absorption near edge structure (XANES) data and (b) extended X-ray absorption fine structure (EXAFS) data (presented as a k^3-weighted Fourier transform) for Mo-doped NM-50/50 compared with Li_2MoO_4 and Li_2MoO_3 standards.

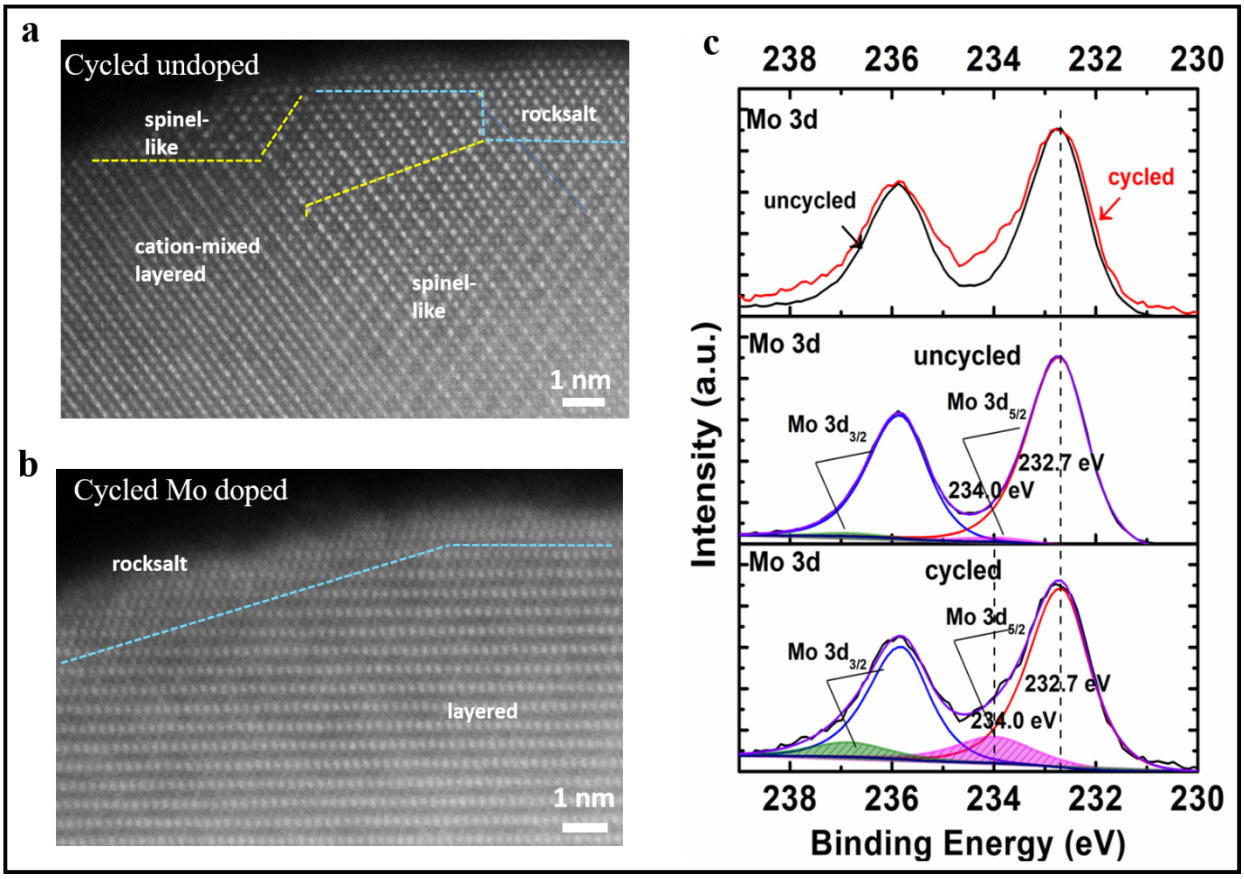

Figure 5. Post-mortem analysis of NM-50/50 and Mo-doped NM-50/50 after 100 charge/discharge cycles. (a-b) HAADF-STEM images of near surface regions showing grain boundaries for (a) NM-50/50 and (b) Mo-doped NM-50/50. (c) XPS analysis showing Mo 3d core-level spectra of pristine and cycled Mo-doped NM-50/50.

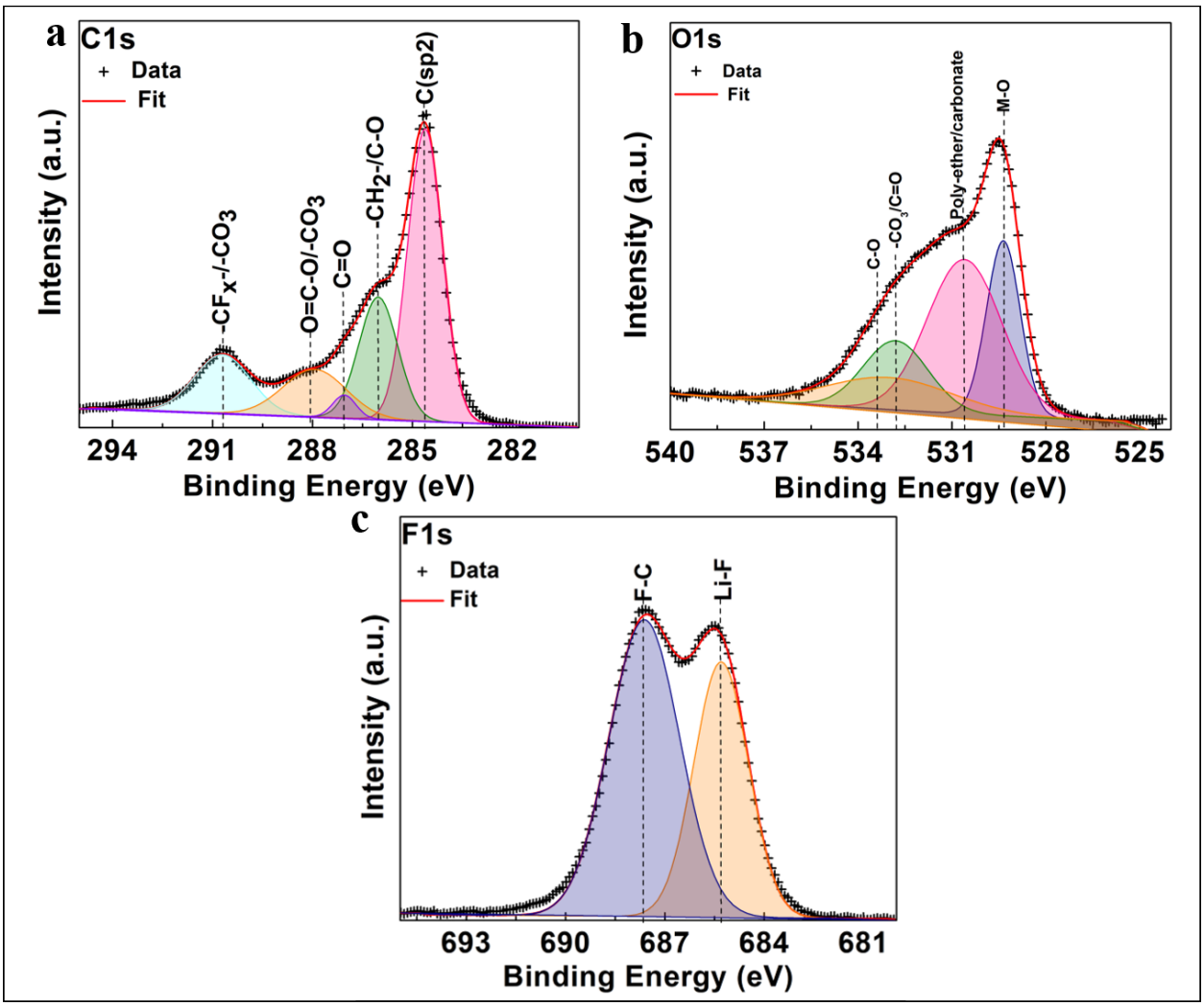

Figure 6. *Ex-situ* XPS results showing (a) C 1s, (b) O 1s, and (c) F 1s core-level spectra for Mo-doped NM-50/50 after 100 cycles. The cathode was harvested after discharging to 2.0 V vs. Li/Li^+.

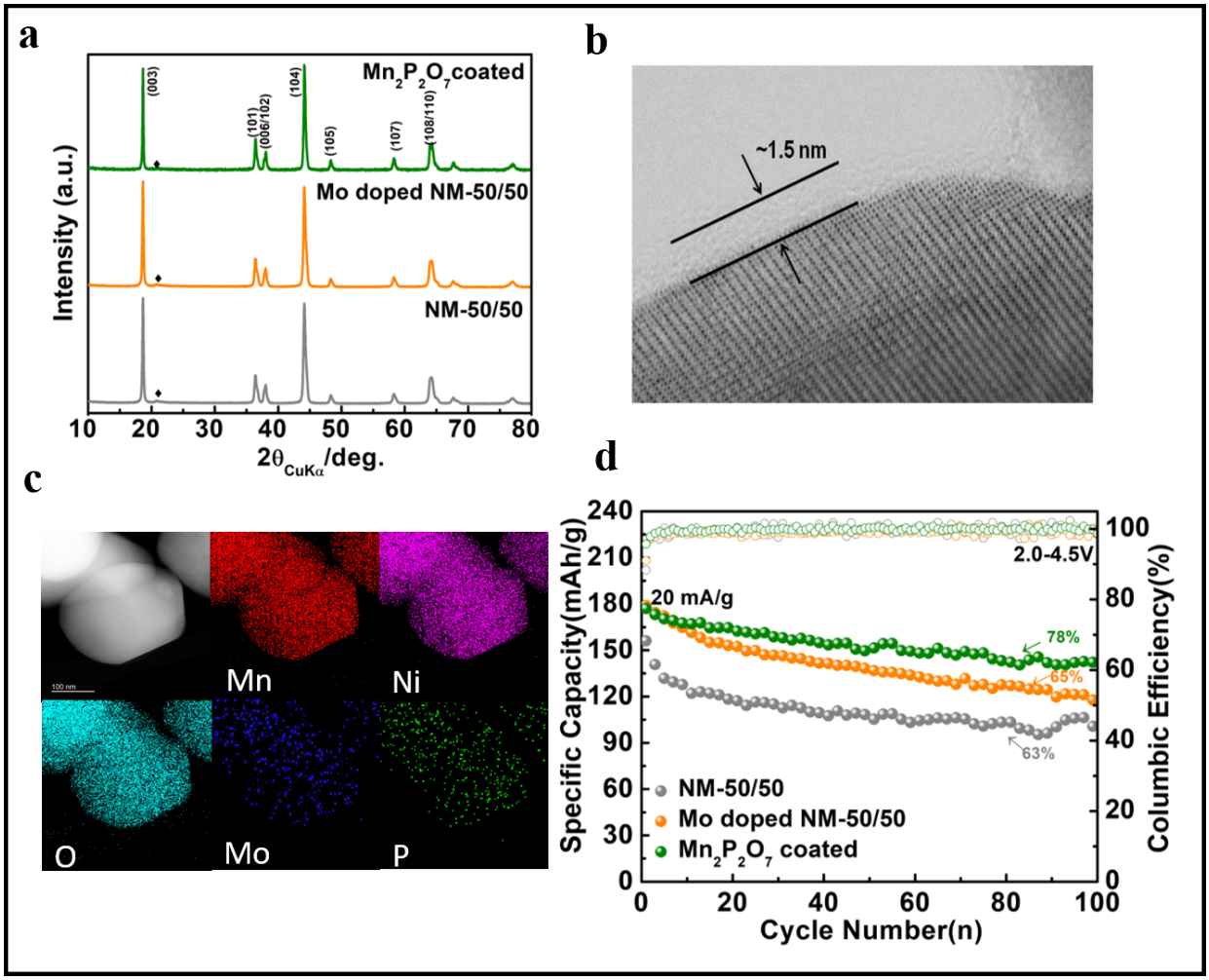

Figure 7. Structural analysis of Mo-doped NM-50/50 coated with 2 wt.% $Mn_2P_2O_7$. (a) XRD patterns of uncoated and coated Mo-doped NM-50/50. (b) ABF-STEM images showing the $Mn_2P_2O_7$ coating is largely amorphous and ~1.5 nm thick. (c) STEM-EDS maps of Mn, Ni, O, Mo, and P. (d) Electrochemical performance of half-cells containing either NM-50/50, Mo-doped NM-50/50, or Mo-doped NM-50/50 coated with 2 wt.% $Mn_2P_2O_7$. The $Mn_2P_2O_7$ coating significantly improved the cathode's cycle life by stabilizing the cathode/electrolyte interface.

Supporting Information

New synthesis strategies to improve Co-Free $LiNi_{0.5}Mn_{0.5}O_2$ Cathodes: Early transition metal d^0 dopants and Manganese Pyrophosphate Coating

Devendrasinh Darbar, Ethan C. Self, Linze Li, Chongmin Wang, Harry M. Meyer III, Changwook Lee, Jason R. Croy, Mahalingam Balasubramanian, Nitin Muralidharan, Indranil Bhattacharya, Ilias Belharouak, Jagjit Nanda**

Table S1. Nominal amounts of precursors used to prepare $LiNi_{0.5}Mn_{0.5}O_2$, $LiNi_{0.5-x/2}Mn_{0.5-x/2}Mo_xO_2$ (x = 0.005 – 0.05), $LiNi_{0.5-x/2}Mn_{0.5-x/2}Ti_xO_2$ (x = 0.01 – 0.05) cathodes.

		Weight (g)			
			Dopant concentration		
Sample	**Precursor**	**Pristine**	**1 at.%**	**3 at.%**	**5at.%**
	$Li(OCOCH_3)_2•2H_2O$ (5 mol% excess)	5.59			
$LiNi_{0.5}Mn_{0.5}O_2$ (5g)	$Ni(OCOCH_3)_2•4H_2O$	6.49			
	$Mn(OCOCH_3)_2•4H_2O$	6.39			
	Citric acid	10.03			
	$Li(OCOCH_3)_2•2H_2O$ (5 mol% excess)		5.57	5.52	5.48
$LiNi_{0.5-x/2}Mn_{0.5-x/2}Mo_xO_2$ (x = 0.005 – 0.05) (5g)	$Ni(OCOCH_3)_2•4H_2O$		6.40	6.22	6.04
	$Mn(OCOCH_3)_2•4H_2O$		6.30	6.13	5.95
	$(NH_4)_6Mo_7O_{24}$		0.09	0.27	0.45
	Citric acid		9.99	9.91	9.83
	$Li(OCOCH_3)_2•2H_2O$ (5 mol% excess)		5.59	5.60	5.61
$LiNi_{0.5-x/2}Mn_{0.5-x/2}Ti_xO_2$ (x = 0.01 – 0.05) (5g)	$Ni(OCOCH_3)_2•4H_2O$		6.43	6.31	6.20
	$Mn(OCOCH_3)_2•4H_2O$		6.34	6.22	6.10
	TiO_2		0.04	0.12	0.20
	Citric acid		10.04	10.06	10.07

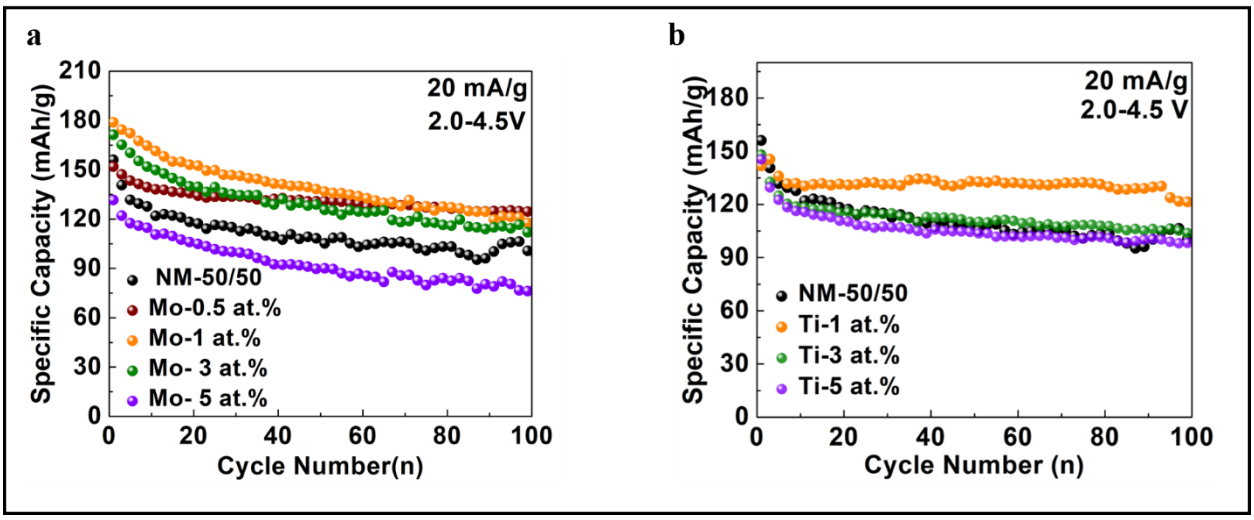

Figure S1. Galvanostatic cycling performance of (a) Mo-doped NM-50/50 containing 0.5 – 5 at.% Mo and (b) Ti-doped NM-50/50 containing 1 – 5 at.% Ti.

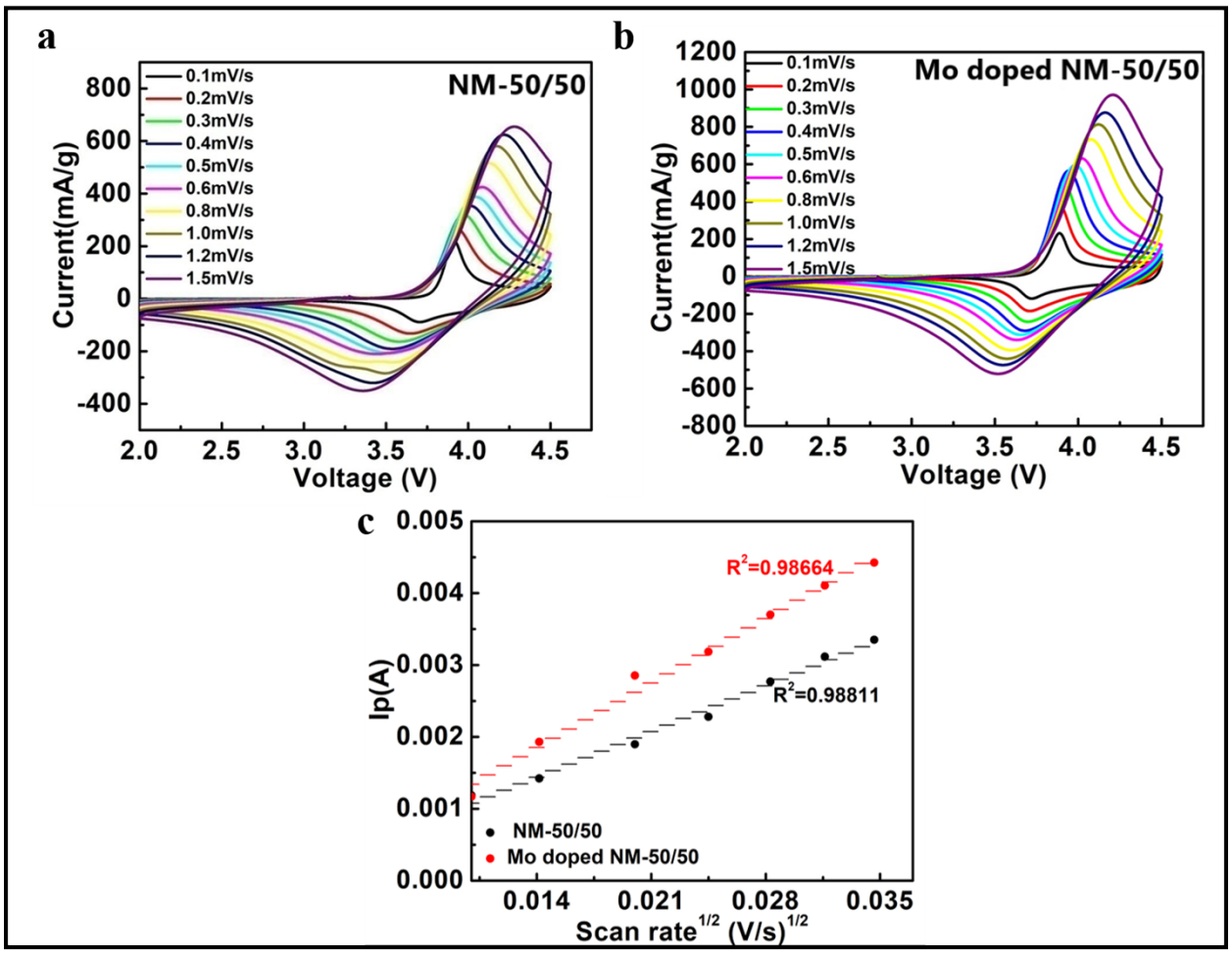

Figure S2. Cyclic voltammograms collected between 2.0 – 4.5 V vs. Li/Li^+ at 0.1 – 1.5 mV/s for (a) NM-50/50 and (b) Mo-doped NM-50/50 cathodes. (c) Anodic peak currents plotted as a function of the square root of the scan rate. The linear relationship in (c) was used to determine the apparent Li^+ diffusion coefficient in the cathodes using a Randles-Sevcik analysis described below.

Calculation of apparent Li^+ diffusion coefficient in NM-50/50 and Mo-doped NM-50/50

The apparent Li^+ diffusion coefficients in NM-50/50 and Mo-doped NM-50/50 cathodes were calculated according to the Randles-Sevcik equation:

$$Ip = 2.68 * 10^5 * n^{3/2} A*D^{1/2*} C*\omega^{1/2} \quad (1)$$

where *Ip* is the anodic peak current after baseline correction (A), n is the number of the involved electrons (n=1), A is the electrode area (cm^2), D is the apparent Li^+ diffusion coefficient ($cm^2\ s^{-1}$), C is the Li^+ concentration in the cathode (0.006440 mol cm^{-3} for NM-50/50 and 0.006028 mol cm^{-3} for Mo-doped NM-50/50), ω is the applied scan rate ($V\ s^{-1}$). Due to difficulties in double-layer baseline corrections during reduction scans, apparent Li^+ diffusion coefficients were only calculated using the anodic peaks (see Table S1). The electrochemically active surface area for the porous electrodes is unknown, and the electrodes' geometric area was used in Equation (1). Furthermore, although Li^+ diffusivity is a function of state of charge, a detailed analysis showing how diffusivity changed with Li^+ concentration is outside the scope of this study. As such, these results should only be used for qualitative comparisons of Li^+ transport in undoped vs. Mo-doped NM-50/50.

Table S2. Calculated apparent Li^+ diffusion coefficients for undoped and Mo-doped NM-50/50 based on the data presented in Figure S2c.

Material	**Apparent Li^+ Diffusion Coefficient ($cm^2\ s^{-1}$)**
NM-50/50	2.9×10^{-9}
Mo-doped NM-50/50	6.7×10^{-9}

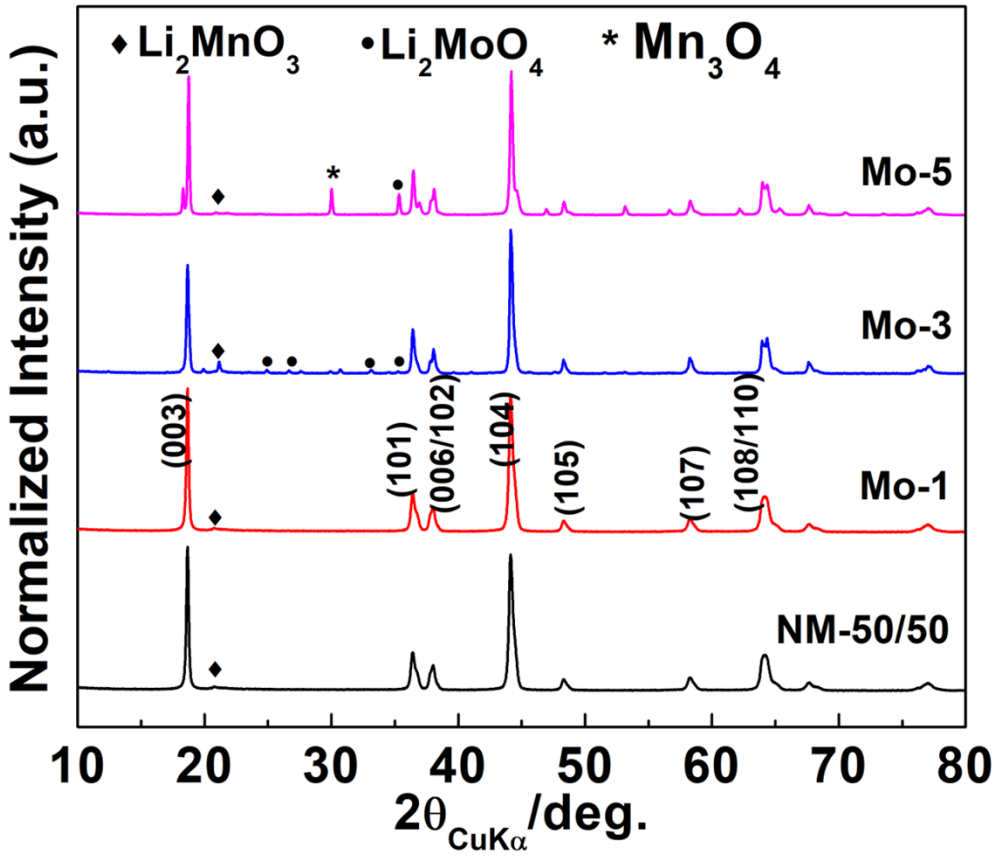

Figure S3. XRD patterns of NM-50/50 containing 0-5 at.% Mo dopant. Higher Mo dopant concentrations led to formation of Li_2MoO_4 and Mn_3O_4 impurities.

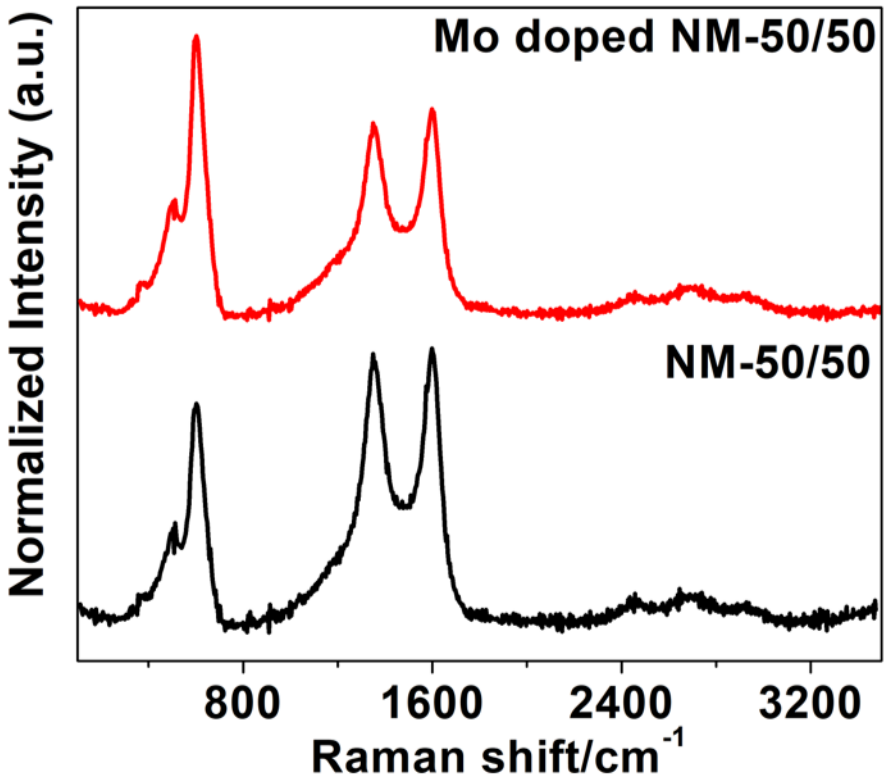

Figure S4. Raman spectra of uncycled of NM-50/50 and Mo doped NM-50/50 cathodes.

Table S3. Surface composition of the NM-50/50 and Mo-doped NM-50/50 (1 at.% Mo) as determined using XPS. Na and S signals are likely due to trace contaminants present in either the glovebox or XPS chamber.

Sample	Surface Composition (at.%)								Mo/(Ni+Mn) Molar Ratio	
	Li	Ni	Mn	Mo	O	C	Na	S	Measured	Expected
NM-50/50 Powder	27.3	6.9	4.5	--	35.3	24.6	0.5	0.9	--	--
Mo-Doped NM-50/50 Powder	25.9	4.5	3.2	1.4	29.3	35.5	0.0	0.3	0.18	0.01

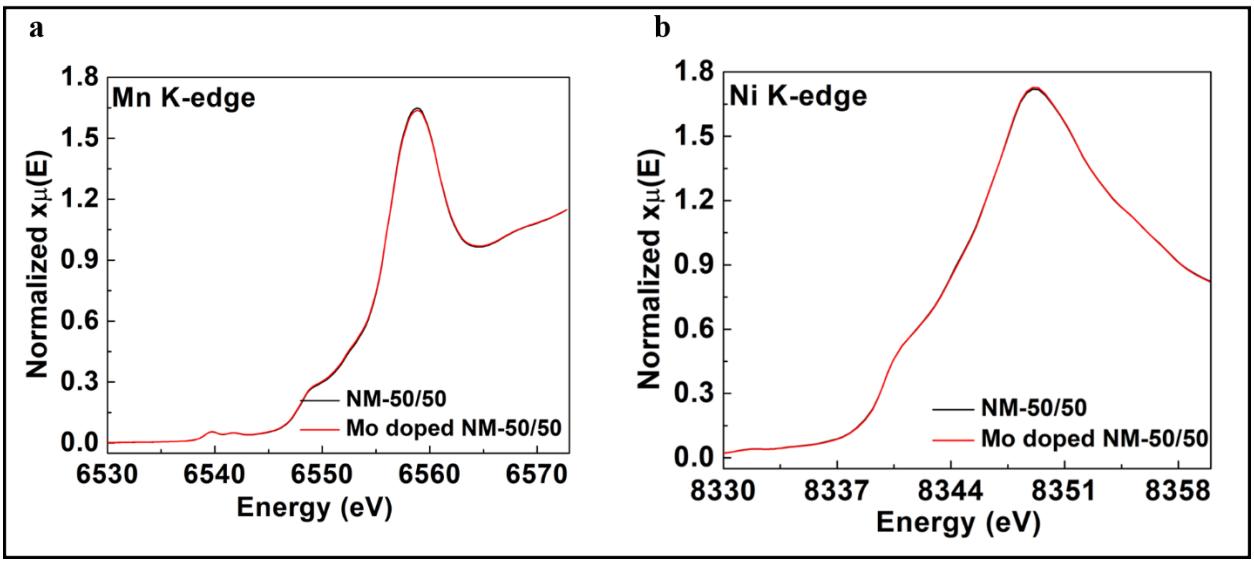

Figure S5. XANES analysis of NM-50/50 and Mo-doped NM-50/50 showing (a) Ni K-edge and (b) Mn K-edge data.

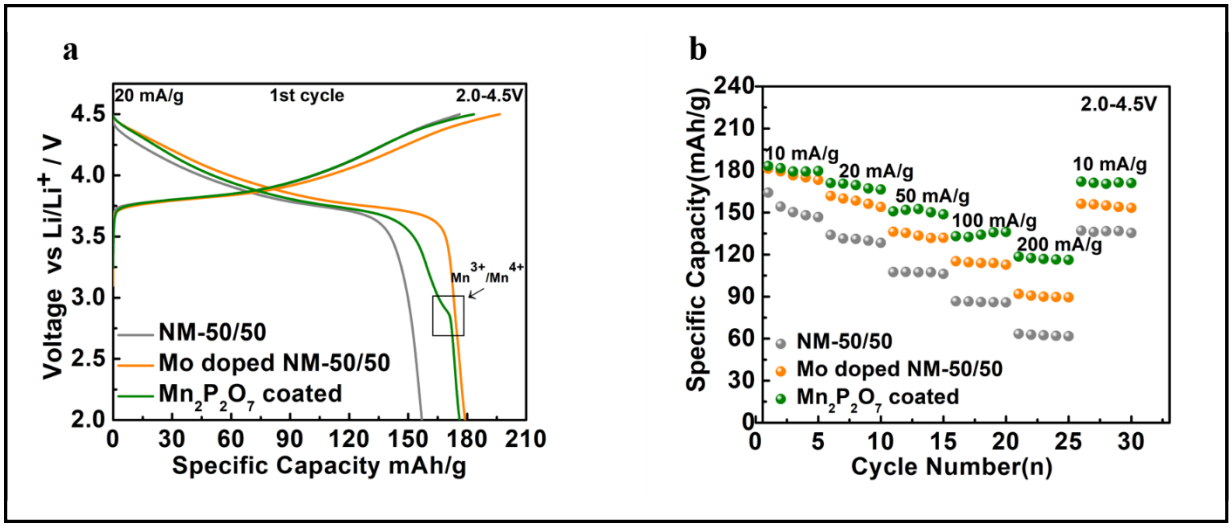

Figure S6. Electrochemical performance of NM-50/50, Mo-doped NM-50/50, and Mo-doped NM-50/50 coated with 2 wt.% $Mn_2P_2O_7$. (a) Galvanostatic charge/discharge curves collected during the first cycle and (b) rate performance collected at specific currents of 10-200 mA/g. Rate capabilities of NM-50/50 and Mo-doped NM-50/50 were reported in our previous work[12].